

Sparse SAR imaging based on $L_{1/2}$ regularization

ZENG JinShan, FANG Jian & XU ZongBen*

Institute for Information and System Sciences & Ministry of Education Key Lab for Intelligent Networks and Network Security, Xi'an Jiaotong University, Xi'an 710049, China

Received March 12, 2012; accepted May 13, 2012

Abstract In this paper, a novel method for synthetic aperture radar (SAR) imaging is proposed. The approach is based on $L_{1/2}$ regularization to reconstruct the scattering field, which optimizes a quadratic error term of the SAR observation process subject to the interested scene sparsity. Compared to the conventional SAR imaging technique, the new method implements SAR imaging effectively at much lower sampling rate than the Nyquist rate, and produces high-quality images with reduced sidelobes and increased resolution. Also, over the prevalent greedy pursuit and L_1 regularization based SAR imaging methods, there are remarkable performance improvements of the new method. On one hand, the new method significantly reduces the number of measurements needed for reconstruction, as supported by a phase transition diagram study. On the other hand, the new method is more robust to the observation noise. These fundamental properties of the new method are supported and demonstrated both by simulations and real SAR data experiments.

Keywords synthetic aperture radar, matched filtering, compressed sensing, $L_{1/2}$ regularization, L_1 regularization

Citation Zeng J S, Fang J, Xu Z B. Sparse SAR imaging based on $L_{1/2}$ regularization. *Sci China Inf Sci*, 2012, 55: 1755–1775, doi: 10.1007/s11432-012-4632-5

1 Introduction

Synthetic aperture radar (SAR) is an active and coherent microwave radar, which produces high spatial resolution images from a moving platform – an airplane or a satellite [1]. It plays an important role in remote sensing, and has been widely used in many military and civilian applications, including target recognition, earth observation, environmental monitoring and surveillance, due to its properties of all weather and day-night imaging.

SAR imaging is an inverse scattering problem whereby a spatial map of reflectivity is reconstructed from measurements of scattered electric fields, and it is normally modeled as an ill-posed linear inverse problem. In conventional SAR imaging, the data acquired are sampled at the Nyquist rate. The Shannon-Nyquist sampling theorem, which suggests that the sampling rate must be at least two times of the signal bandwidth in order to get a lossless recovery of the band-limited real signal. According to the principle of high-resolution radar [2], the range and azimuth resolutions of a SAR image are directly proportional to the bandwidth of the transmitted signal and the doppler bandwidth, respectively. In order to obtain a high radar resolution, therefore, a wide transmitted signal bandwidth in range and a wide synthetic

*Corresponding author (email: zbxu@mail.xjtu.edu.cn)

doppler bandwidth in azimuth are needed; thus the sampling rates in both range and azimuth must be very high. This leads to a much more onboard memory and downlink throughput required for the platform.

The recently emerging field of compressed sensing (CS) suggests that it is possible to recover a sparse or compressible image from a small number of random measurements with an appropriate nonlinear reconstruction procedure [3,4]. Unlike the conventional sampling way, CS is a procedure of using the sparsity of the signal and combining sampling with compression, which permits signals to be sampled at the sub-Nyquist rate and recovered from the compressed measurements. Inspired by the CS theory, many methods for SAR imaging have been reported [5–7]. A compressive radar imaging scheme based on the CS notation was firstly reported by Baraniuk et al. [6]. They employed orthogonal matching pursuit (OMP) algorithm [8] for radar imaging from the compressed measurements. In [5], Alonso et al. focused on the SAR raw data, and used the regularized OMP (ROMP) [9] to implement SAR imaging. The OMP and ROMP, however, both are greedy pursuit algorithms, which can be quite fast, especially in the ultrasparsity regime, while they are inefficient or even fail when the signal is not very sparse and heavy observational noise is present [10].

Another important class of algorithms, named as L_p regularization, were also utilized for radar imaging [11–14]. The simplest and most common approach is L_2 regularization. When minimizing a quadratic function of the unknown quantities, this approach degenerates to Tikhonov regularization [15,16]. In [13], a regularized inversion method is proposed for stripmap-mode SAR, which involves deconvolution of the projections of the field by Tikhonov-type regularization, followed by backprojection. The method leads to a straightforward optimization problem, but suppresses useful features in the resulting imagery, such as edges. One improved method based on non-quadratic penalty (namely, L_p regularization with $p \in (0, 2)$) for SAR imaging was proposed to preserve such features in [11], with extension to passive radar for multiple transmitters in [12]. Specially, when $p \leq 1$, many advantages over conventional radar imaging including enhanced features, increased resolution and reduced sidelobes were demonstrated in [11]. The L_1 regularization is advocated for radar imaging in [14], promoted as an alternative strategy for L_0 regularization in compressed sensing [3,4]. Since L_1 regularization is a convex problem, it can be very efficiently solved [17–19] (Particularly, it permits an analytic thresholding representation [20]). Under some conditions, the resultant solution of L_1 regularization coincides with one of the solutions of L_0 regularization (L_1/L_0 equivalence) [21,22]. Because of these, the L_1 regularization gets its popularity and has been accepted as a most useful tool for solving the sparsity problems. Nevertheless, while L_1 regularization provides the best convex approximation to L_0 regularization and it is computationally efficient, the L_1 regularization cannot enforce further sparsity when applied to compressed sensing, hence limiting the practical efficacy of L_1 regularization for SAR imaging.

Despite the wide use of L_1 regularization, the sparsity promoting ability of the L_1 regularization and its performance when applied to SAR imaging, have not been thoroughly investigated. In recent years, L_q ($0 < q < 1$) regularization was introduced as a further improvement upon performance of L_1 regularization, since L_q regularization can assuredly generate much sparser solutions than L_1 regularization [23–25]. Nevertheless, L_q regularization is a non-convex, non-smooth and non-Lipschitz optimization problem. It is difficult in general to have a thorough theoretical understanding and fast algorithms for solving this problem. Moreover, even if the problem is solvable, which q should be selected to yield a best result is also a problem. Instead of considering the generic L_q regularization schemes, the $L_{1/2}$ regularization was specially analyzed in [24–27]. The representativeness of $L_{1/2}$ regularization among the L_q regularizations with q in $(0, 1)$ was revealed according to the phase transition study in [26]. The study shows that the $L_{1/2}$ regularization is at least as good as any other L_q regularization with $q \in (0, 1)$, and it definitely has stronger sparsity-promoting capability than L_q regularization with any $q \in (1/2, 1]$. Furthermore, a thresholding representation theory for $L_{1/2}$ regularization and a fast solver, called the iterative half thresholding algorithm, for solving $L_{1/2}$ regularization were then established [25].

Inspired by the advantages of L_q ($0 < q < 1$) regularization and the well developed theoretical properties of $L_{1/2}$ regularization, we suggest a novel method for SAR imaging based on $L_{1/2}$ regularization theory in this paper (called $L_{1/2}$ -SAR imaging method hereinafter). We will show that if the interested scene

is sparse or compressible, a high-quality SAR image with increased resolution and reduced sidelobes can be obtained through applying so-suggested new SAR imaging method even when far fewer number of measurements are adopted than needed in the conventional SAR systems, the greedy pursuit and L_1 regularization based systems. The robustness of the proposed method to the observation noise can also be verified.

The reminder of the paper is organized as follows. In Section 2, we propose a new method for SAR imaging based on $L_{1/2}$ regularization and conduct a necessary analysis of it. In Section 3, several fundamental features of the proposed method are justified and tested through a series of simulations. In Section 4, two real SAR data experiments are presented to validate the proposed method. The conclusion is then presented in Section 5 with some useful remarks.

2 SAR imaging based on $L_{1/2}$ regularization

In this section, we present a SAR imaging method based on $L_{1/2}$ regularization, and then give an intuitive illustration of the new method. We then present a detailed comparison of the previous work with the proposed method.

2.1 SAR observation model

In this subsection, we formulate the observation model of the stripmap-mode SAR [1].

The ground-plane geometry for stripmap-mode SAR is shown as Figure 1. This acquisition geometry provides data along a terrain strip parallel to the flight direction (i.e., azimuth direction). The radar platform travels at velocity v in the azimuth direction and transmits wideband microwave pulses at regular intervals. The corresponding echoes are recorded. Many pulses are transmitted during the so-called integration time, i.e., the time the platform takes to travel the footprint cross-range length. More specifically, a complex baseband pulse $s(\tau)$, usually chirp, is modulated in quadrature by a carrier frequency f_0 to yield the transmitted waveform $p(\tau) = \text{Re}\{s(\tau)e^{j2\pi f_0\tau}\}$. Then $p(\tau)$ is transmitted at the uniform pulse repetition interval (PRI), where $\text{Re}\{\cdot\}$ denotes the real part of $\{\cdot\}$. The received backscattered energy can be modeled as a convolution of the pulse waveform with the ground reflectivity function $f(\tau, \eta)$, where τ , η represent the fast (range) and slow (azimuth) times, respectively. Upon receiving, the echo is then quadrature demodulated to the complex baseband signal $y_r(\tau', \eta')$, that is,

$$y_r(\tau', \eta') = \iint f(\tau, \eta)g(\tau', \eta' - \eta; \tau)d\tau d\eta + u(\tau', \eta'), \quad (1)$$

where $g(\tau', \eta' - \eta; \tau) = \omega_\tau(\tau' - \frac{2R(\tau, \eta' - \eta)}{c})\omega_\eta(\eta')s(\tau - \frac{2R(\tau, \eta' - \eta)}{c})e^{-j4\pi f_0 R(\tau, \eta' - \eta)/c}$, and c is the speed of light, ω_τ is the envelop function of transmitted pulse in range, ω_η is the antenna beam pattern in azimuth, $R(\tau, \eta' - \eta) = \sqrt{(c\tau/2)^2 + [v(\eta' - \eta)]^2}$ is the slant range between radar and the target, $u(\tau', \eta')$ is assumed to be the white Gaussian noise arising from thermal noise in the transmitter and receiver hardware.

Furthermore, we sample the continuous-time analog echo $y_r(\tau', \eta')$ with the additive complex white Gaussian noise $u(\tau', \eta')$ at the grid of time (τ_k', η_l') , $k = 1, \dots, K$ and $l = 1, \dots, L$, and discretize the reflectivity field $f(\tau, \eta)$ at the grid of time (τ_i, η_j) , $i = 1, \dots, M$ and $j = 1, \dots, N$. Thus we obtain the following SAR observation model:

$$y = Af + u, \quad (2)$$

where $y \in \mathbb{C}^m$, $f \in \mathbb{C}^n$, $A \in \mathbb{C}^{m \times n}$, $u \in \mathbb{C}^m$, $m = KL$ and $n = MN$. More specifically, $y_{k+(l-1)K} = y_r(\tau_k', \eta_l')$, $f_{i+(j-1)M} = f(\tau_i, \eta_j)$, $u_{k+(l-1)K} = u(\tau_k', \eta_l')$, and $A_{(k+(l-1)K), (i+(j-1)M)} = g(\tau_k', \eta_l' - \eta_j; \tau_i)$. The SAR imaging problem is how to reconstruct the reflectivity f from (2).

2.2 $L_{1/2}$ -SAR imaging

We propose the following new method for SAR imaging based on $L_{1/2}$ regularization.

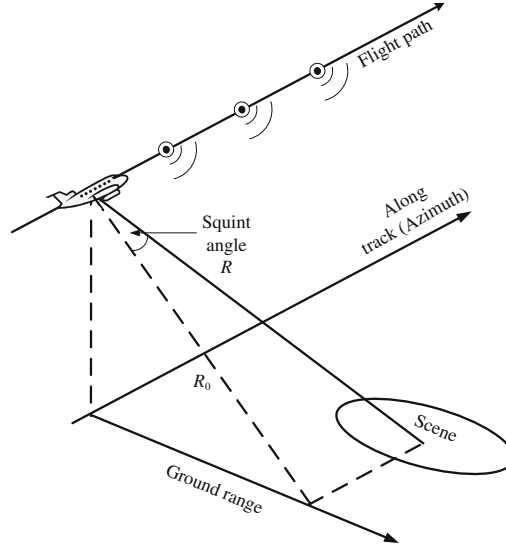


Figure 1 SAR data acquisition geometry of stripmap-mode SAR.

Consider the sampled linear model (2), and assume that the reflectivity f is sparse under a basis $\Psi \in \mathbb{C}^{n \times n}$ with the sparse representation x . Then linear model (2) can be rewritten as

$$y = Af + u = A\Psi x + u = \Phi x + u, \quad (3)$$

where $\Phi = A\Psi$ and $f = \Psi x$. According to Eq. (3), take the $L_{1/2}$ quasi-norm, $\|x\|_{1/2}^{1/2} = \sum_{i=1}^n \sqrt{|x_i|}$, as the sparsity measure. Then the SAR imaging problem (3) can be formulated as the following $L_{1/2}$ -norm minimization problem:

$$\min_{x \in \mathbb{C}^n} \|x\|_{1/2}^{1/2} \quad \text{subject to} \quad \|y - \Phi x\|_2 < \epsilon, \quad (4)$$

which can be further transformed into the following so-called $L_{1/2}$ regularization problem:

$$x^* = \operatorname{argmin}_{x \in \mathbb{C}^n} \{\|y - \Phi x\|_2^2 + \lambda \|x\|_{1/2}^{1/2}\}, \quad (5)$$

where $\lambda > 0$ is the regularization parameter.

The first term in objective function (5) is a data fitting term, which corresponds to linear model (3), and hence the information about the observation geometry. The second term in (5) incorporates prior information regarding the behavior of the filed f in the transform domain Ψ , and the nature features of interested scene in the resulting reconstruction.

The naïve approach for solving the complex SAR imaging problem (3) is to convert it into the corresponding real problem through dividing x , y and Φ into their real and imaginary parts, since most early developed sparse recovery methods could only deal with the real problems. In practice, this does not work well for sparse cases, and in principle the approach is questionable because it does not minimise the $L_{1/2}$ -norm of the complex signal [28].

In order to get a solution of the complex-valued $L_{1/2}$ regularization problem (5), we extend the half thresholding representation theory established on the real space [25] to the complex space. By similar derivations, it can be shown that the half thresholding representation theory still holds in the complex case. That is, the solutions of problem (5) can be analytically expressed in a thresholding form, i.e., any solution x of the complex-valued $L_{1/2}$ regularization problem (5) can be expressed as

$$x = H_{\lambda\mu, 1/2}(B_\mu(x)), \quad (6)$$

where $B_\mu(x) = x + \mu\Phi^H(y - \Phi x)$, μ is an arbitrary positive real parameter, and $H_{\lambda\mu, 1/2}(\cdot)$ is the complex-valued half thresholding operator defined by

$$H_{\lambda\mu, 1/2}(x) = (h_{\lambda\mu, 1/2}(x_1), \dots, h_{\lambda\mu, 1/2}(x_n))^T. \quad (7)$$

Here, for any $z \in \mathbb{C}$, $h_{\lambda\mu,1/2}(z)$ is defined by

$$h_{\lambda\mu,1/2}(z) = \begin{cases} \frac{2}{3}z \left(1 + \cos \left(\frac{2\pi}{3} - \frac{2}{3}\varphi_{\lambda\mu}(z) \right) \right), & |z| > \frac{\sqrt[3]{54}}{4}(\lambda\mu)^{2/3}, \\ 0, & \text{otherwise,} \end{cases} \quad (8)$$

where $\varphi_{\lambda\mu}(z) = \arccos(\frac{\lambda\mu}{8}(\frac{|z|}{3})^{-\frac{3}{2}})$. With the thresholding representation (6)–(8), a complex-valued iterative half thresholding algorithm for resolving problem (5) can be given by

$$x_{n+1} = H_{\lambda_n\mu_n,1/2}(B_{\mu_n}(x_n)). \quad (9)$$

Assume x^* is a solution of the problem (5) with k -sparsity (that is, the number of nonzero components of x^* is k). Then the optimal regularization parameter λ^* satisfies

$$\lambda^* \in \left[\frac{\sqrt{96}}{9\mu}(|B_{\mu}(x^*)|_{k+1})^{3/2}, \frac{\sqrt{96}}{9\mu}(|B_{\mu}(x^*)|_k)^{3/2} \right), \quad (10)$$

where $|B_{\mu}(x^*)|_k$ represents the k th largest component of $B_{\mu}(x^*)$ in magnitude. This leads to a nearly optimal regularization parameter setting strategy for implementing algorithm (9):

$$\lambda_n = \frac{\sqrt{96}}{9\mu}(|B_{\mu}(x_n)|_{k+1})^{3/2}, \quad (11)$$

where $\{x_n\}$ is an iterative sequence defined by (9).

As in [25], the convergence of the complex-valued iterative half thresholding algorithm (9) can be verified when parameter μ satisfies $\mu \in (0, 1/\|\Phi\|_2^2)$. This, together with (11), provides a fixed parameter setting strategy of algorithm (9).

It is noted that the computational complexity of the proposed method is of the same order as Φ or its adjoint per iteration; that is, the computational complexity per iteration is $O(mn)$. Also, an attractive characteristic of the new method is that it does not require explicit operations on the matrix Φ , but only requires that one apply the operators Φ and Φ^H to any given vector.

2.3 An intuitive illustration on $L_{1/2}$ -SAR imaging

It is observed that when Ψ is the identity matrix and the initial value x_0 is set to zero, the first update $B_{\mu_0}(x_0) = x_0 + \mu_0\Phi^H(y - \Phi x_0)$ becomes $B_{\mu_0}(x_0) = \mu_0 A^H y$, which is a scale of the matched filter output [7] with a constant $\mu_0 \in (0, 1)$. Thus the first iteration of (9) in this case gives

$$x_1 = H_{\lambda_0\mu_0,1/2}(B_{\mu_0}(x_0)) = H_{\lambda_0\mu_0,1/2}(\mu_0\mathcal{X}), \quad (12)$$

where $\mathcal{X} = A^H y$ is the matched filter output, $H_{\lambda_0\mu_0,1/2}(\cdot)$ is the half thresholding operator with parameter $\lambda_0\mu_0$. With this observation, the proposed SAR imaging method (9) can be viewed as a finer update of the conventional matched filtering, driven by the scene sparsity.

In the next subsection, we will show that the proposed new approach (5)–(11) has many advantages, over the traditional matched filtering based SAR imaging method as well as some other sparse SAR imaging methods. However, we will present an intuitive illustration below on how the new approach brings a benefit of producing images with reduced sidelobes and increased resolution. We show this through analyzing the case of SAR imaging for single point scatterer (see, Figure 2). For simplicity, we assume that the transmitted signal $s(t)$ is a Chirp signal, which is the most commonly used transmitted signal in SAR imaging applications. In this case, the output of matched filter is a sinc function (that is, $\text{sinc}(x) = \frac{\sin(\pi x)}{\pi x}$) approximately as shown in Figure 2(a), and the outputs of the first iteration of approach (12) with different regularization parameters ($\lambda_0 = 0.025, 0.075$ and 0.125) and fixed $\mu_0 = 1$ are shown in Figures 2 (b), (c) and (d). To evaluate the severity of the aliasing artifacts, we calculate the peak-to-sidelobe ratio (PSR) of different outputs. The PSRs of first iteration outputs of the approach

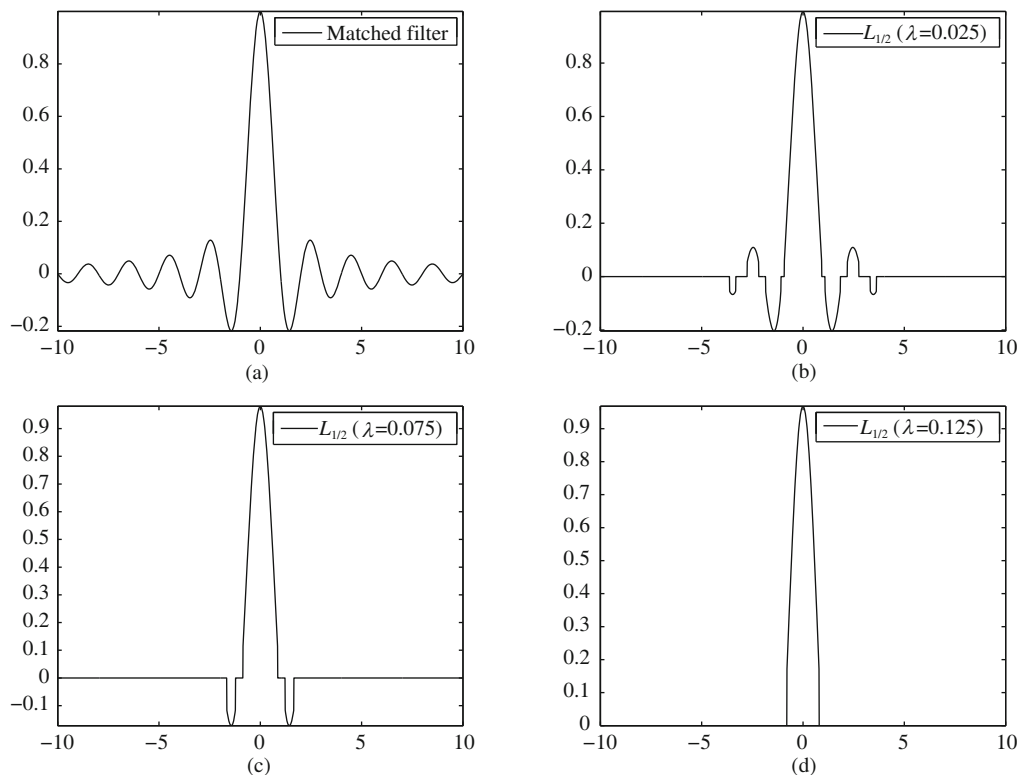


Figure 2 The outputs for single point scatterer yielded by matched filter and the first iteration outputs of the new method with different regularization parameters. (a) The matched filter output (PSR=13.2 dB); (b) the new method output with $\lambda = 0.025$ (PSR=14 dB); (c) the new method output with $\lambda = 0.075$ (PSR=15.4 dB); (d) the new method output with $\lambda = 0.125$ (PSR=Inf dB).

with different regularization parameters are clearly higher than those of the matched filter output, and the PSR increases monotonically with the regularization parameter, as shown in Figure 2. We can see from Figure 2 that a noticeable effect of our approach, is the absence of sidelobes, as well as higher resolution than the matched filtering, as the width of the mainlobe gets narrower, through choosing a suitable regularization parameter as shown in Figure 2(d).

2.4 Relationships with previous works

In this subsection, we briefly discuss the relationship between the proposed method and the nonquadratic regularization based SAR imaging method proposed by Cetin et al. [11] (called Cetin method hereinafter), while the relationships with the conventional, as well as some other known sparse SAR imaging methods, will be demonstrated in the next section.

In [11], the following SAR imaging model was proposed:

$$x^* = \operatorname{argmin}_{x \in \mathbb{C}^n} \{ \|y - \Phi x\|_2^2 + \lambda_1 \|x\|_q^q + \lambda_2 \|D|x|\|_q^q \}, \quad (13)$$

where $q \in (0, 2)$, $\|\cdot\|_q^q$ denotes L_q -norm, D is a discrete approximation to the 2-D derivative operator (gradient), $|x|$ denotes the vector of magnitudes of the complex-valued vector x , λ_1 and λ_2 are regularization parameters. $\|x\|_q^q$ and $\|D|x|\|_q^q$ have been used to enhance the point-based and region-based features, respectively.

Since it is generally intractable to solve (13) directly, the following approximated model was suggested as a substitution of (13),

$$x^* = \operatorname{argmin}_{x \in \mathbb{C}^n} \left\{ \|y - \Phi x\|_2^2 + \lambda_1 \sum_{i=1}^n (|x_i|^2 + \epsilon)^{q/2} + \lambda_2 \sum_{i=1}^n (|(D|x|)_i|^2 + \epsilon)^{q/2} \right\}, \quad (14)$$

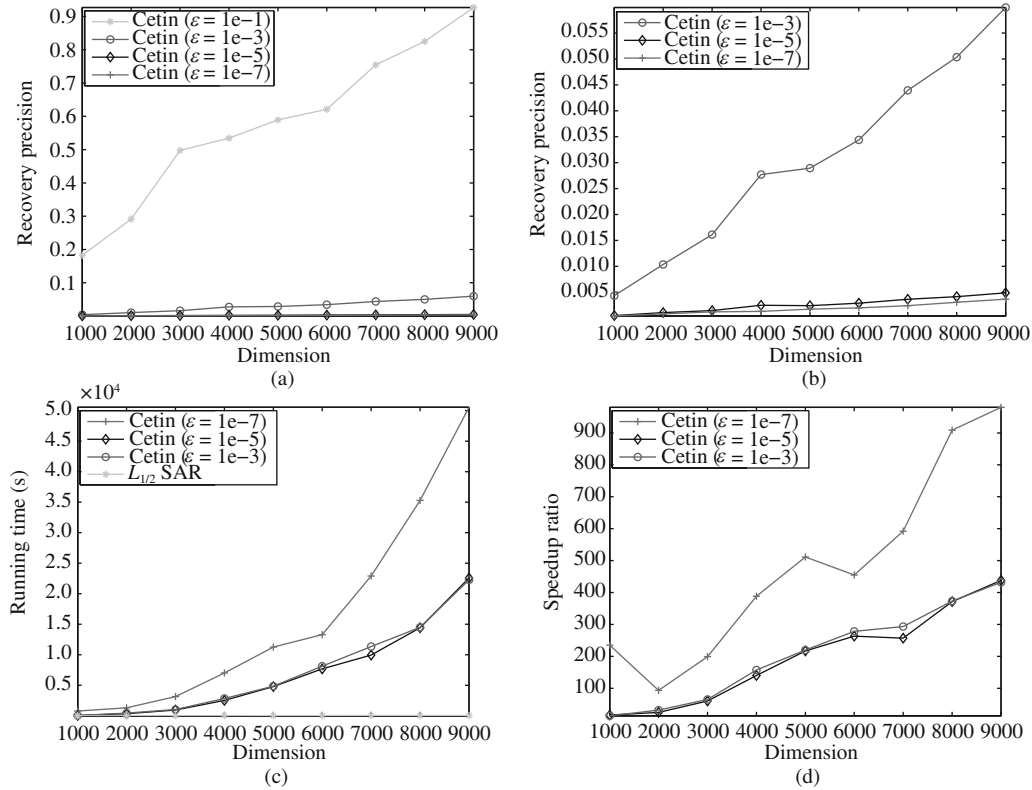


Figure 3 The influence of parameter ϵ for Cetin method, and the comparison on the running time between the $L_{1/2}$ -SAR imaging method and Cetin method. Except ϵ , the other parameters in Cetin method were set to be $q = 1/2$, $\lambda_1 = 1$, $\lambda_2 = 0$ and $\gamma = 1$. (a) Recovery precisions of Cetin method; (b) detailed comparison on recovery precisions of Cetin method; (c) comparison on the running time between the $L_{1/2}$ -SAR method and Cetin method with different ϵ ; (d) speedup ratio of the running time brought by the $L_{1/2}$ -SAR method, as compared to Cetin method with different ϵ .

where $\epsilon > 0$ is a small constant. The model (14) could be solved efficiently through the quasi-Newton based iterative approach [11].

The relationship between Cetin method (13), (14) and the proposed $L_{1/2}$ -SAR imaging method (5)–(11) can be summarized as follows.

(i) Cetin method is conceptually applicable to much wider scope of problems that allow to incorporate the sparsity of gradient domain of interested scene, in addition to the sparsity of scene. Nevertheless, when applied to the case where many point scatterers exist (the gradient then does not make sense), model (13) degenerates to the well-known L_q regularization approach

$$x^* = \operatorname{argmin}_{x \in \mathbb{C}^n} \{ \|y - \Phi x\|_2^2 + \lambda_1 \|x\|_q^q \}. \quad (15)$$

It is well known that when $q > 1$, the above model does not yield sparse solution in general. When $q \leq 1$, the model does yield sparse solution and, the smaller q , the sparser the solutions defined by the model. In practical applications, therefore, how much q should be is a crucial problem when Cetin method is used. The $L_{1/2}$ -SAR imaging method we suggested in the last section uses the fixed index $q = 1/2$. This specific choice is not only free from the setting issue of q faced in Cetin method, but also rooted in solid analysis on the representativeness of $q = 1/2$ in terms of yielding the most sparse solution [26]. Furthermore, a well developed theory on $L_{1/2}$ regularization exists [25], which allows the $L_{1/2}$ regularization to be solved very efficiently.

(ii) Besides the model parameter q , there are many other parameters, such as λ_1 , λ_2 and ϵ that need to be present. Without a definite rule (they are chosen based on a subjective qualitative assessment of the formed imagery, as reported in [11], the effectiveness of Cetin method relies on the parameters critically. For example, Figure 3 shows the influence of parameter ϵ upon the precision of reconstructed scenes when

Table 1 Radar parameter settings of the point target simulation

Parameter Name (Notation)	Setting (Unit)
Slant range of scene center (R_c)	10 (km)
Effective radar velocity (V_r)	350 (m/s)
Transmitted pulse duration (T_r)	2 (μ s)
Radar center frequency (f_0)	3 (GHz)
Signal bandwidth (B_r)	50 (MHz)
Antenna aperture (L_a)	4 (m)
Beam squint angle ($\theta_{sq,c}$)	0 ($^\circ$)

Cetin method is applied to 1-D simulated SAR imaging experiments. It is seen that when ϵ was taken to be relatively big (say, $\epsilon = 1e - 1$), Cetin method (14) does not yield an reasonable approximated solution, while when ϵ is relatively smaller (say, $\epsilon = 1e - 7$), the method can give a good approximated solution, but the computational complexity is significantly increased, (Figures 3 (c) and (d)), since problem (14) gets ill-conditioned. How to properly set parameter ϵ is a crucial and difficult issue in Cetin method. Nevertheless, the $L_{1/2}$ -SAR imaging method is much simpler than Cetin method with only two parameters (λ and μ), which can be selected directly according to the given rule, derived from the well developed $L_{1/2}$ regularization theory.

(iii) Cetin method is an approximated L_q regularization approach (actually, based on model (14) but not (13)), while the $L_{1/2}$ -SAR imaging method is an exactly $L_{1/2}$ regularization approach. In Cetin method, model (14) is solved via the well-known quasi-Newton iteration, while in $L_{1/2}$ -SAR imaging method, model (5) is solved by a fast thresholding iterative method (9)–(11). As demonstrated in Figures 3 (c) and (d), the $L_{1/2}$ -SAR imaging method is generally much faster than Cetin method (in the case shown in Figure 3 (d), the $L_{1/2}$ -SAR method brings an approximately 100 times speed-up of Cetin method). Such a speed-up can be more remarkable as the dimensions increase.

Figure 3 shows the experiment results of Cetin method and $L_{1/2}$ -SAR imaging method, when applied to a series of 1-D simulated SAR imaging applications with different parameters (k, m, n) of SAR model (3). In this experiment, $k = 50$, $m = 1000$, and n varies from 1000 to 9000. The synthetic 1-D scene is k -sparsity with unit reflectivity magnitude and random phase. The termination conditions of both the proposed and Cetin methods are set to $\|x^{t+1} - x^t\|_2 / \|x^t\| < 1e - 3$. The recovery precision ($RecP$) is defined as $RecP = \|\hat{x} - x^*\|_2 / \|x^*\|_2$, where x^* and \hat{x} represent the truth scene and the recovery, respectively.

3 Fundamental properties of $L_{1/2}$ -SAR imaging

In this section, some fundamental properties of $L_{1/2}$ -SAR imaging method, including high-quality imaging with increased resolution and reduced sidelobes, the reconstruction ability from compressed measurements and robustness to the observation noise, are studied and verified by a series of simulation experiments. The outperformance of the new method is demonstrated by comparing with the traditional matched filtering, greedy pursuit and L_1 regularization based methods. More specifically, For greedy pursuit based SAR imaging methods, we will apply the orthogonal matching pursuit (OMP) algorithm [8], which is one of the most well-known greedy algorithms, for SAR imaging. Moreover, for L_1 regularization based methods, we will employ the fast iterative shrinkage-thresholding algorithm (FISTA) [17] for SAR imaging. This is adequate since it is known that FISTA is an essential L_1 regularization algorithm which is efficient for high-dimensional problems (this is crucial for SAR imaging application).

All these experiments were implemented in a personal computer (2.51 GHz, 127 GB of RAM, quad-core AMD opteron(tm) processor 8380) with MATLAB 7.12.0 platform (R2011a).

3.1 Point target simulation

In order to demonstrate the superiorities of the new method we have conducted a point target simulation whose main parameters for simulation are listed in Table 1.

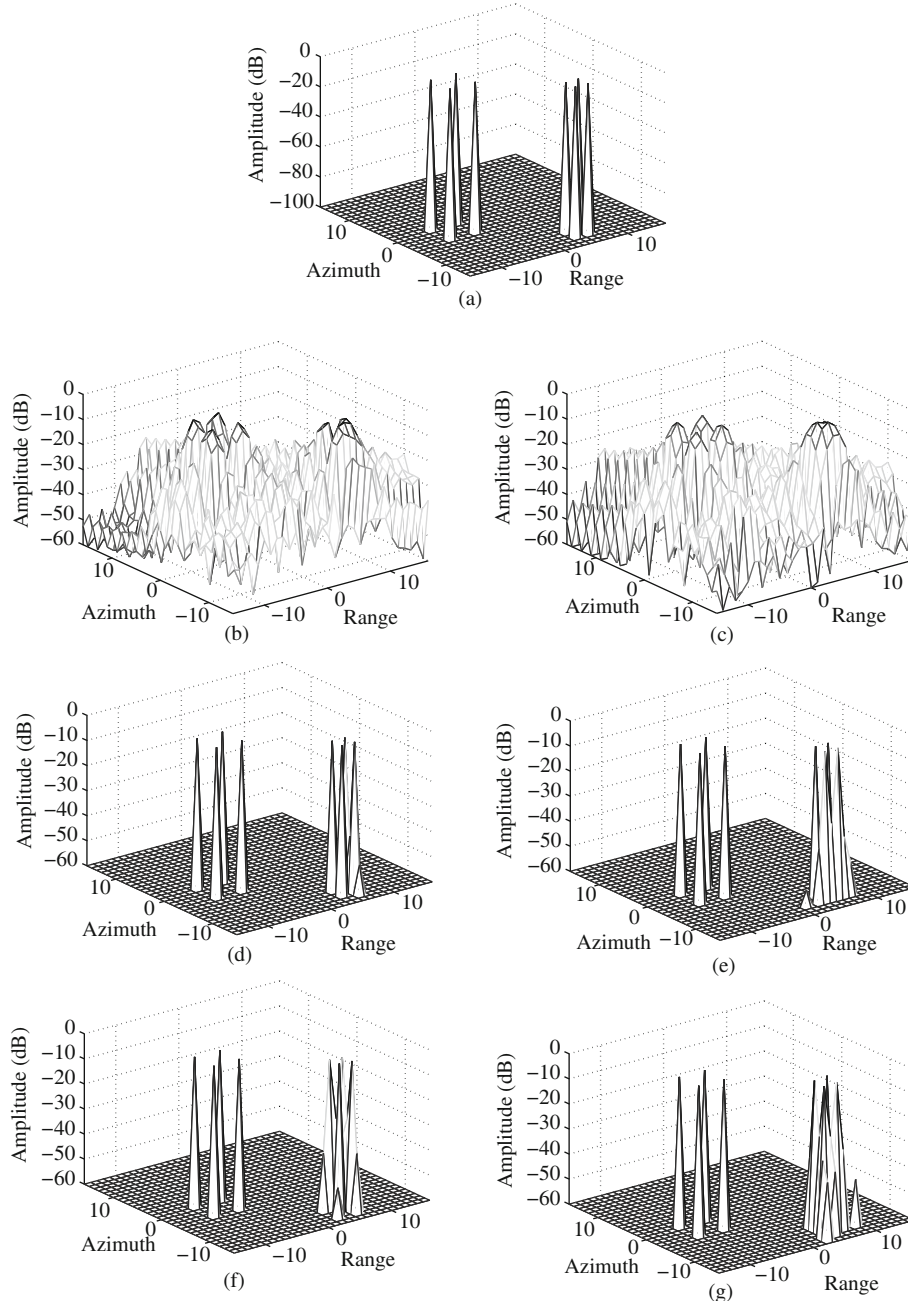


Figure 4 Mesh plots of the point target simulation results of the conventional SAR imaging method and the new method when applied to SAR imaging with different noise levels and under different sampling rates. (a) Synthetic scene; (b) conventional method without noise under full sampling rate; (c) conventional method with 20 dB noise under full sampling rate; (d) the new method without noise under full sampling rate; (e) the new method with 20 dB noise under full sampling rate; (f) the new method without noise under 30% sampling rate; (g) the new method with 20 dB noise under 30% sampling rate.

The synthetic scene with 200×300 pixels composes eight single-pixel scatterers with unit reflectivity magnitude and random phase. The 3D mesh plot of the magnitude of the interested target region with 32×32 pixels is shown in Figure 4 (a). We simulated SAR echoes from this ideal scene such that the bandwidth of the signal supports a resolution cell of 2×2 pixels. We applied the conventional matched filtering and the proposed $L_{1/2}$ -SAR imaging method to SAR imaging from the received echoes at both noiseless case and Gaussian noise case with 20 dB. Moreover, we implemented the new method for SAR imaging at both full sampling rate (i.e., the Nyquist rate) and 30% sampling rate. The simulation results

of the interested target region with 32×32 pixels are shown in Figure 4.

As shown in Figure 4, the conventional method cannot distinguish the right region of four scatterers at both noiseless and noise cases, since these four scatterers fall into one resolution cell, and the recovery clearly suffers from high sidelobes, as shown in Figures 4 (b) and (c). However, the proposed method implements SAR imaging effectively at both cases under the full sampling rate. As shown in Figures 4 (d) and (e), all the scatterers are resolved, sidelobes are suppressed and peak reflectivity magnitudes are preserved (the standard deviations of the magnitudes are 0.0101 and 0.0134 in (d) and (e), respectively). Furthermore, the new method produces high-quality images at much lower sampling rate (30%) than the Nyquist rate, as shown in Figures 4 (f) and (g). Thus, the simulation demonstrates the fundamental properties of the new method such as the superresolution capability and sidelobes suppression, as compared to the conventional SAR imaging method. Also, the reconstruction ability under the sub-Nyquist rate and the robustness of the proposed method are observed.

3.2 SAR imaging based on sub-Nyquist rate

Furthermore, in order to check the reconstruction ability and robustness of the proposed SAR imaging method, we implemented one-dimension (1-D) simulated SAR imaging under different sampling rates and noise levels. The influence of the sampling rate and the additive noise on the new method was analyzed through comparison with the conventional matched filtering.

The simulations were implemented by the subsequent way. First, the round-trip delay for a collection of point targets was randomly generated using a uniform distribution corresponding to a range of valid distances. Then, the complex scattering coefficient of each target was randomly chosen from a Rayleigh distribution in amplitude and a uniform distribution in phase. Finally, the received signal was generated as the sum of the time-shifted replicas of the transmitted waveform (which was adjusted to be a chirp signal), with each being multiplied by its respective scattering coefficient. Once the received signal was synthesized, a random white Gaussian noise vector was added to simulate the thermal noise. Specifically, we generated an n -length ($n=1024$) 1-D target scene with k -sparsity ($k=64$, that is, the number of nonzero components is 64) according to the way described above. We considered different sampling rates and noise levels in terms of signal-to-noise-ratio (SNR) from -10 dB to 40 dB compared with the matched filtering. The recovery performance was then qualitatively measured with the recovery SNR (rSNR), which is defined by

$$\text{rSNR} = 20 \log_{10} \frac{\|x\|_2}{\|x^* - x\|_2}, \quad (16)$$

where x is the ground-truth scene and x^* is the corresponding recovery. In each case, we implemented 30 independent realizations, and the average rSNR out of the 30 realizations was taken as the final result. The recovery results are shown in Figure 5.

As shown in Figure 5, the recovery SNR gets better and better as the noise SNR level increases. When the SNR of the noise level is higher than 10 dB, the recovery SNR of the new method is better than matched filtering even under the sampling rate 30%, as shown in Figure 5 where the blue solid line is above the black dotted line with plus. It is interesting to notice that the recovery SNR of matched filtering increases much more slowly than the new method, which is approximately a linear increasing, and the recovery SNR of matched filtering is approaching to a constant value when the noise SNR level increases to some extent (say, 25 dB in this case), since the main factor influencing the recovery SNR is not the additive noise but the sidelobes introduced by matched filtering itself. These results indicate that the new method can implement high-quality SAR imaging at a much lower sampling rate than the Nyquist rate, which is requested for the conventional matched filtering.

3.3 Phase transition diagram

The phase transition diagram was firstly introduced by Donoho et al. [21,22] to provide a way of checking L_1/L_0 equivalence, indicating how sparsity and indeterminacy affect the success of L_1 regularization,

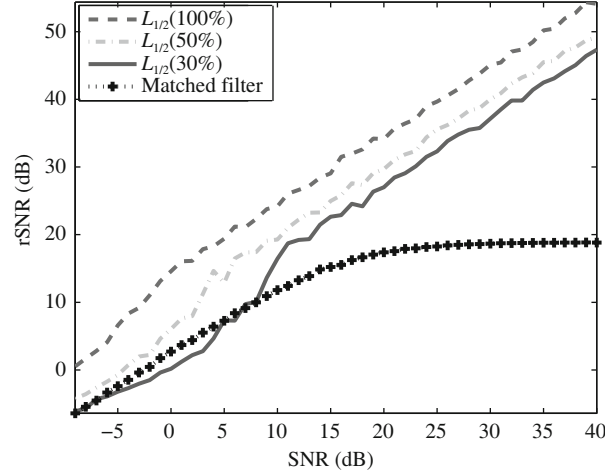


Figure 5 The recovery results of the new method at different sampling rates and matched filtering recovery results with different noise levels from -10 dB to 40 dB. The dashed line, dashdotted line and solid line represent the recovery SNR of the new method under the sampling rates 100% , 50% and 30% , respectively. The dotted line with plus represents the recovery SNR of matched filtering.

and later it was extended as an experiment tool to study the equivalence of L_q/L_0 ($0 < q < 1$) [26] and comparing the ability of sparse reconstruction of different compressed sensing strategies [29]. We propose to apply this tool to evaluate the performance of the proposed method for SAR imaging and compare it with both OMP and L_1 regularization based SAR imaging methods. Let $\delta = m/n$ be the normalized measure of undersampling factor and $\rho = k/m$ be the normalized measure of sparsity. A plot of the pairing of variables δ and ρ describes a two-dimensional phase space $(\delta, \rho) \in [0, 1]^2$. With those notations, we implemented a series of simulation runs by taking the values of δ and ρ at 40 equispaced points in the phase space ($n = 1600$). At each point on the grid, corresponding to a SAR imaging model (3) with different setting of (k, m, n) (in this case $\Psi = I$ and $n = 1600$), the average of the relative mean square error (RMSE) of 30 independent realizations was recorded, and a phase transition diagram of each method was then draw based on these results. The phase transition diagrams of OMP, L_1 regularization based and the new imaging methods are shown in Figure 6.

The first and second column of figures in Figure 6 show the phase transition diagrams in the noiseless case and noise case with with 10 dB Gaussian noise, respectively. These plots indicate that the original target scene can be reconstructed well by the new method as long as it is sufficiently sparse and enough measurements are taken. Furthermore, compared to both OMP and L_1 regularization based methods, the new method uses fewer measurements to reconstruct the scene with the same sparsity, and can reconstruct much denser scene effectively when the same measurements are taken, as demonstrated by Figure 6. From another point of view, we can see that the new method always has better sparse reconstruction ability than both OMP and L_1 regularization based imaging method, as it demonstrates that the successful reconstruction regions (the blue regions) of Figures 6 (e) and (f) are obviously larger than those of (a), (b) and (c), (d) respectively. More specifically, we calculate the percentages of the blue regions in the squares, of which the grid values are less than 0.3 . The percentages of the blue regions of Figures 6 (a)–(f) are 41.81% , 30.34% , 43.56% , 31.19% , 53.13% , and 40.69% respectively. Both in the noiseless and noise cases, in terms of the percentage of the successful reconstruction region, it turns out that there exists more than 10% and 9% improvements of the new method compared to both OMP and L_1 regularization based methods, respectively.

3.4 Robustness to noise

In this subsection, we demonstrate the robustness of the new method to measurement noise. We reconstructed the sparse scene by the new method from compressed measurements at different sampling rates $r = m/n$ and adding complex white Gaussian noise with different SNRs. A plot of the pairing of variables

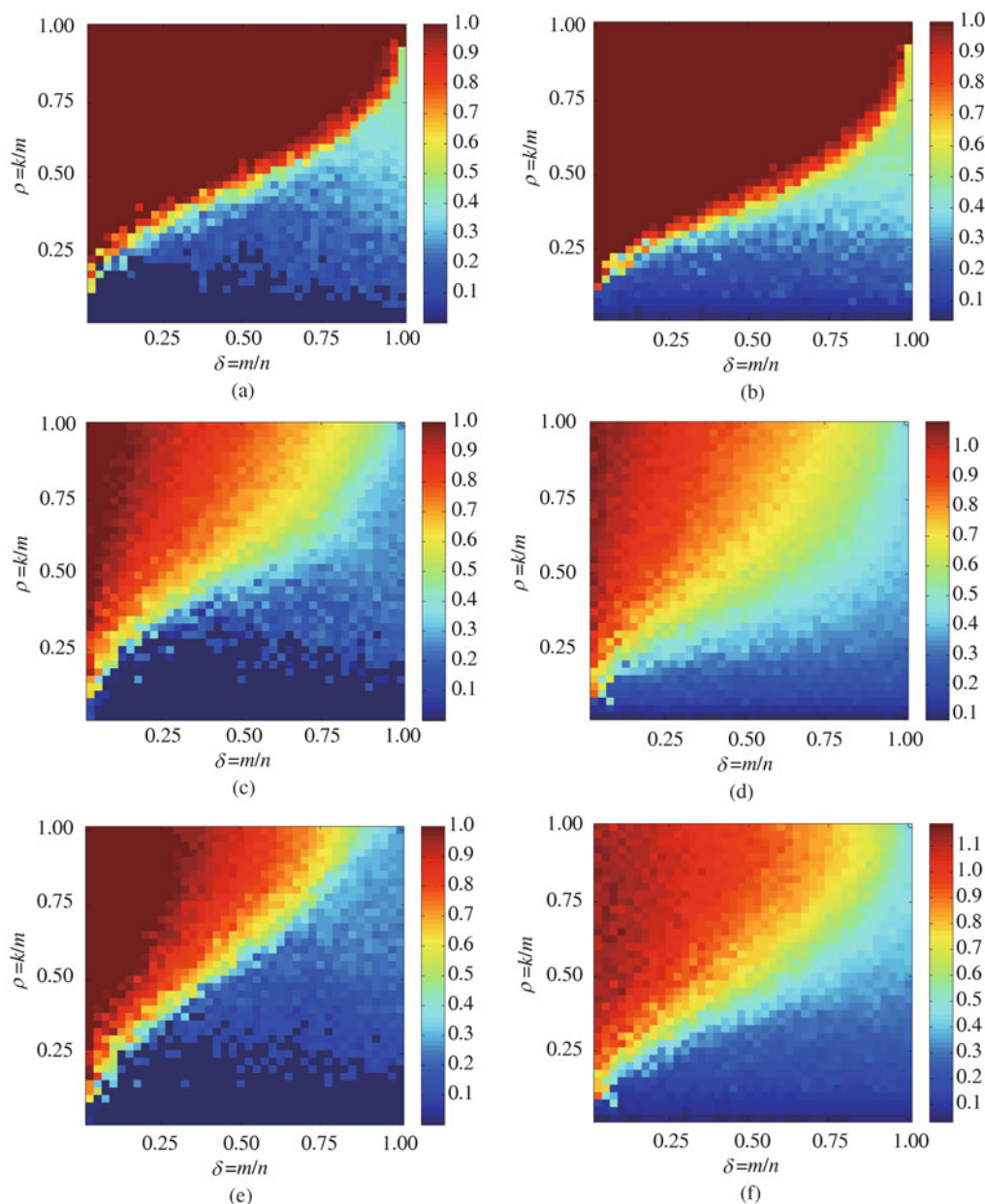


Figure 6 The phase transition diagrams of OMP, L_1 regularization based SAR imaging methods and the new method when applied to SAR imaging. (a) The OMP based method without noise; (b) the OMP based method with 10 dB Gaussian noise; (c) the L_1 regularization based method without noise; (d) the L_1 regularization based method with 10 dB Gaussian noise; (e) the new method without noise; (f) the new method with 10 dB Gaussian noise.

SNR and sampling rate r describes a two-dimension space (SNR, r) . We implemented a series of simulations by taking the values SNR and r ranged through 40 equispaced points in the interval $(-10, 30]$ and $(0, 1]$, respectively. The dimension of the original scene is n ($n = 1600$) and the sparsity is k ($k = 16$). We generated the original scene randomly according to the way described in the Subsection 3.2. At each point on the grid, corresponding to a SAR imaging model (3) with different settings of (m, n, SNR) (in this case $\Psi = I$ and $n = 1600$), the results of OMP, L_1 regularization based and the new methods are presented in Figure 7.

Figures 7 (a), (b) and (c) show the robust reconstruction results of OMP, L_1 regularization based and the new methods from the noisy compressed measurements with different SNRs, respectively. These plots indicate that the new method is more robust than both OMP and L_1 regularization based methods. On one hand, as shown in Figure 7, we can see that under the same noise level, the new method needs fewer

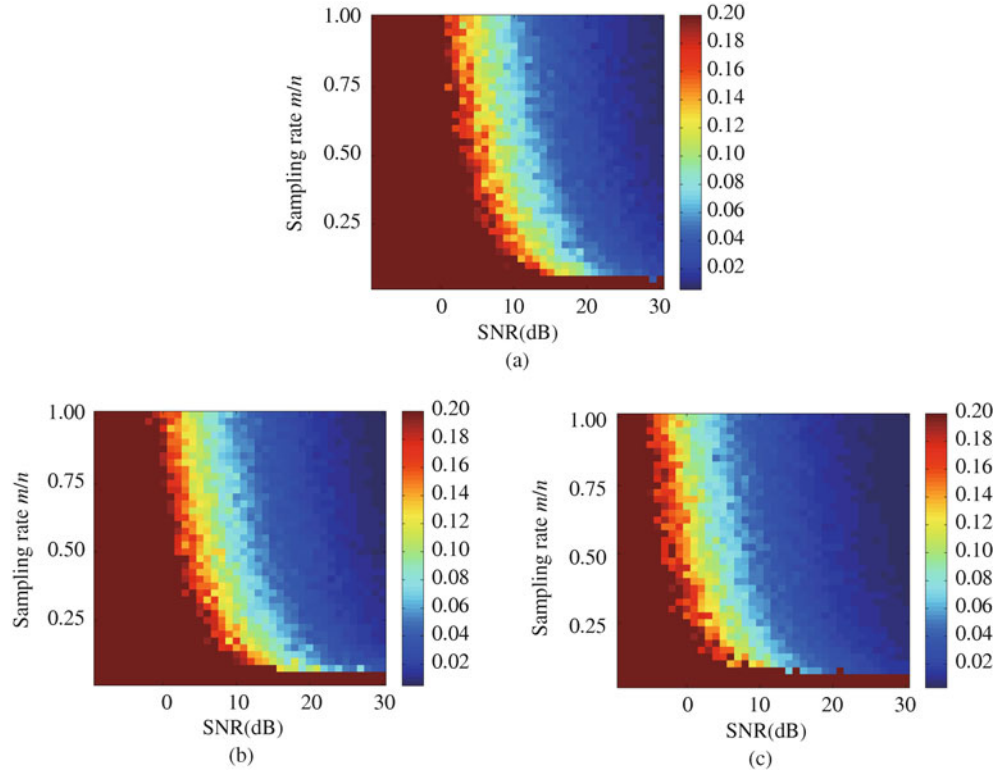


Figure 7 Robust reconstruction from noisy compressed measurements with different SNR corresponding to OMP, L_1 regularization based and the new methods. (a) OMP based method; (b) L_1 regularization based method; (c) the new method. The details are better seen by zooming on a computer scene.

measurements to the effective reconstruction. On the other hand, the new method can reconstruct the original scene from noisy compressed measurements with lower SNR (about 5 dB reduction) than both OMP and L_1 regularization based methods. Furthermore, we calculate the percentages of the successful regions (the blue regions), of which the grid values are less than 0.05. The percentages of the blue regions of Figures 7 (a), (b) and (c) are 35.50%, 36.81% and 49.69%, respectively. It brings a more than 12.5% improvement of the new method over both OMP and L_1 regularization based methods, which confirms that the SNR of data allowing for successful reconstruction of the new method is about 5 dB lower than that of both OMP and L_1 regularization based imaging methods.

4 Real SAR data experiments

In this section, we demonstrate the effectiveness of the new method to real SAR data. We compare the new method with the traditional SAR imaging method to show the improvements achieved. We also compare the new method with both OMP and L_1 regularization based methods from different measurements to show the outperformance of the new method. Specifically, besides the aforementioned three sparse SAR imaging methods, we apply range Doppler algorithm (RDA) [30,31], one of the most commonly used traditional SAR imaging methods, for SAR imaging. These two real SAR data are acquired from ground-based SAR (called, GB-SAR) and RADARSAT-1, respectively.

4.1 Ground-based SAR data reconstruction

We implemented the aforementioned SAR imaging methods for ground-Based SAR data, which was acquired by the advanced scanning two-dimensional railway observation ground-based SAR system of the Institute of Electronics, Chinese Academy of Sciences (called, IECAS-ASTRO Ground-Based SAR system). The interested scene composes three corner reflectors, shown as Figure 8 (a). Some related

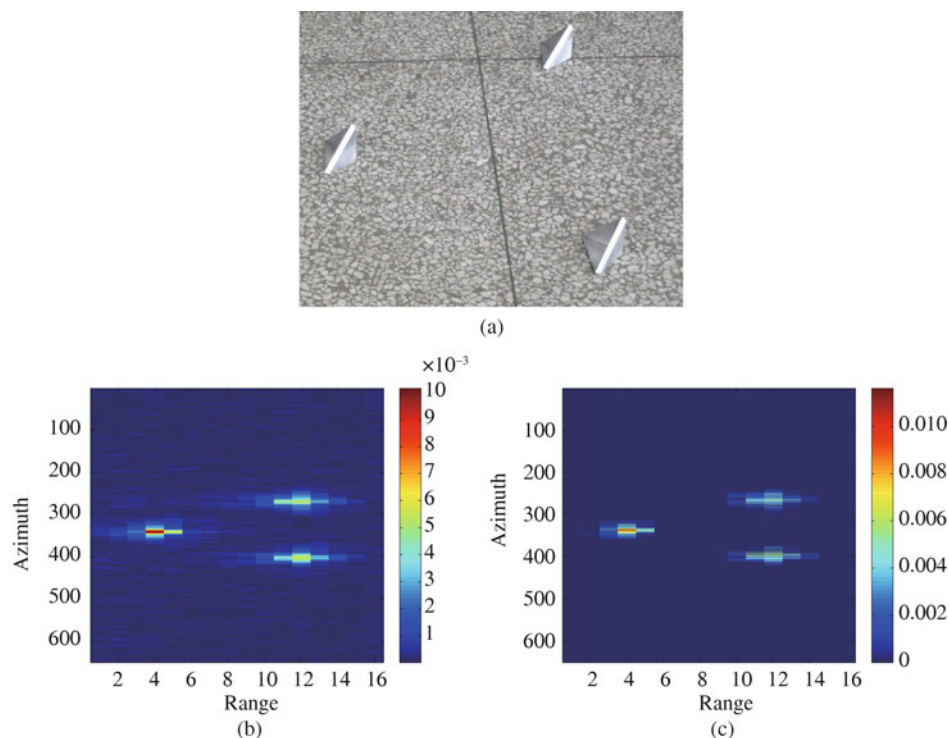


Figure 8 Reconstruction results of Ground-Based SAR data via RDA and the new method. (a) The original SAR scene with three corner reflectors; (b) the traditional SAR reconstruction via RDA using 651 pulses, which is sampled at the traditional Nyquist rate; (c) the reconstruction results of the new method using 651 pulses.

radar parameters are set as follows: the signal bandwidth is 4 GHz with carrier frequency 17 GHz, corresponding to a range resolution of 0.0375m. The pulse repetition frequency is 250 Hz, i.e., 651 pulses within dwell time $[-1.3, 1.3]$ (s) are used in this experiment. The reconstruction results via RDA and the proposed method of using 651 pulses are shown in Figures 8 (b) and (c), respectively. Also, the mesh plots of the traditional SAR and $L_{1/2}$ -SAR reconstruction results using 651 pulses are shown in Figure 9.

As shown in Figure 8, the $L_{1/2}$ -SAR image is much better with the higher resolution and reduced sidelobes than the traditional SAR image. Specially, the background of the $L_{1/2}$ -SAR image is much smoother with fewer artifacts. The superiorities of $L_{1/2}$ -SAR imaging method including increased resolution and reduced sidelobes are further demonstrated by Figure 9. As shown in Figure 9, the 3-D mesh plots of the traditional SAR image via RDA and the $L_{1/2}$ -SAR image are shown in the first and second column of the figures, respectively. As shown in Figures 9 (a) and (b), $L_{1/2}$ -SAR image has higher resolution and smoother background than the traditional SAR image, which is shown more explicitly by Figures 9 (c) and (d). As shown in Figure 9 (c), the sidelobe of the traditional SAR image is about -30 dB, while the sidelobe of $L_{1/2}$ -SAR image is much lower than -60 dB as shown in Figure 9 (d). Furthermore, detailed comparisons about the region 1 (the left reflector) and region 2 (the right two reflectors) of the target scene are shown in Figures 9 (e) to (h). It further demonstrates that the resolutions of the region 1 and region 2 images reconstructed by $L_{1/2}$ -SAR imaging method are much higher than the traditional SAR image. Also, the sidelobes are suppressed efficiently via the new method.

Furthermore, we applied these sparse SAR imaging methods to the GB-SAR data by the use of different number of pulses including 651, 130 and 65. A part of reconstruction results of these methods are shown in Figure 10. The corresponding running time of these sparse SAR imaging methods is shown in Table 2. As shown in Table 2, the new method is much faster than the OMP based SAR imaging method, and almost as fast as the L_1 regularization based method. More specifically, the running time the new method is about half of the OMP based method. In general, the running time of three sparse imaging methods decreases as the number of the pulses used reduces.

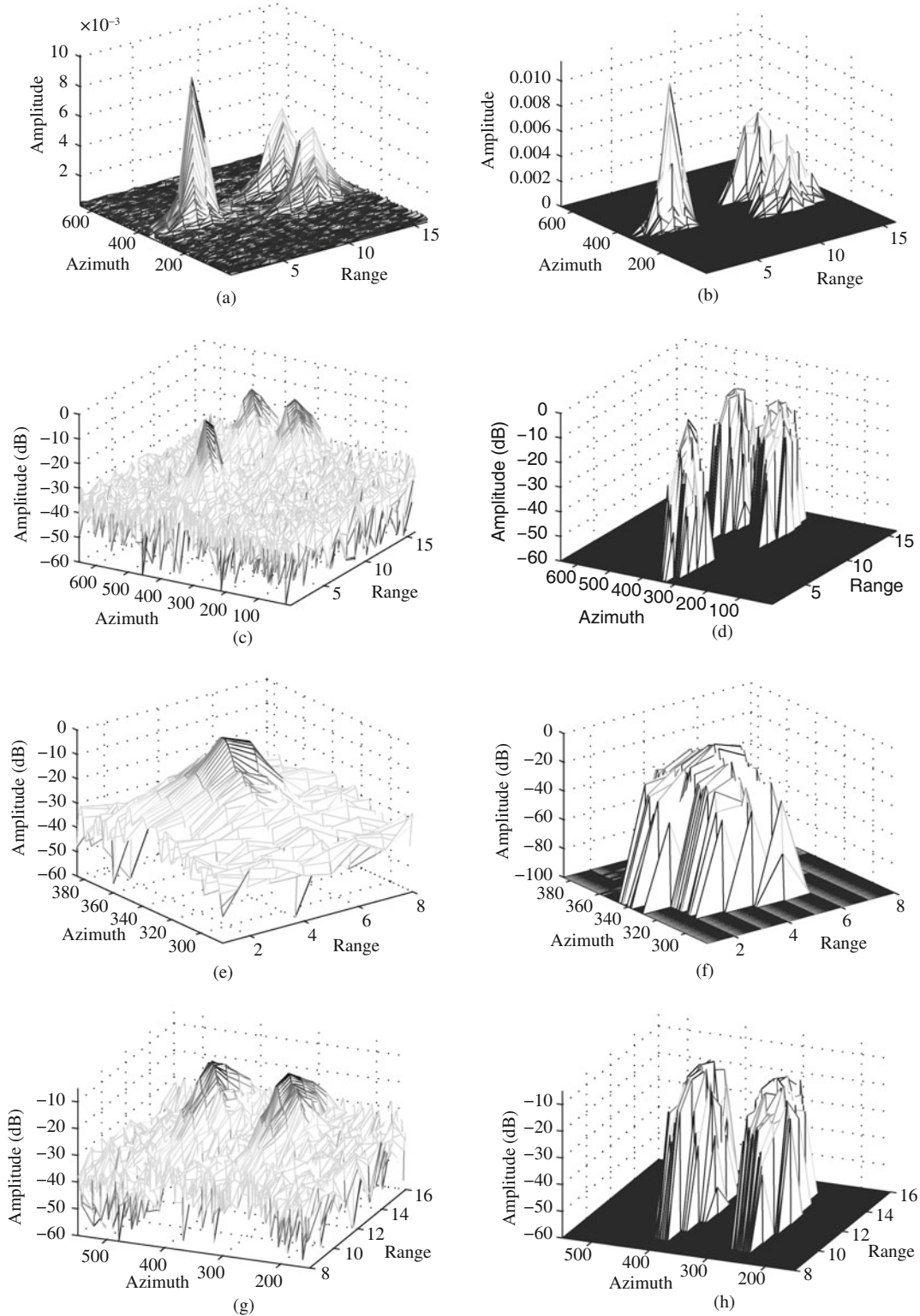


Figure 9 3-D mesh plots of the reconstruction results of Ground-Based SAR data via RDA and $L_{1/2}$ -SAR imaging method using 651 pulses. The first and second rows represent the mesh plots of the SAR images via RDA and $L_{1/2}$ -SAR imaging method, respectively. (a) The traditional SAR image without any scale transform of amplitude; (b) $L_{1/2}$ -SAR image without any scale transform of amplitude; (c) the traditional SAR image with amplitude transformed in dB; (d) $L_{1/2}$ -SAR image with amplitude transformed in dB; (e) region 1 of the traditional SAR image in dB; (f) region 1 of the $L_{1/2}$ -SAR image in dB; (g) region 2 of the traditional SAR image in dB; (d) region 2 of the $L_{1/2}$ -SAR image in dB.

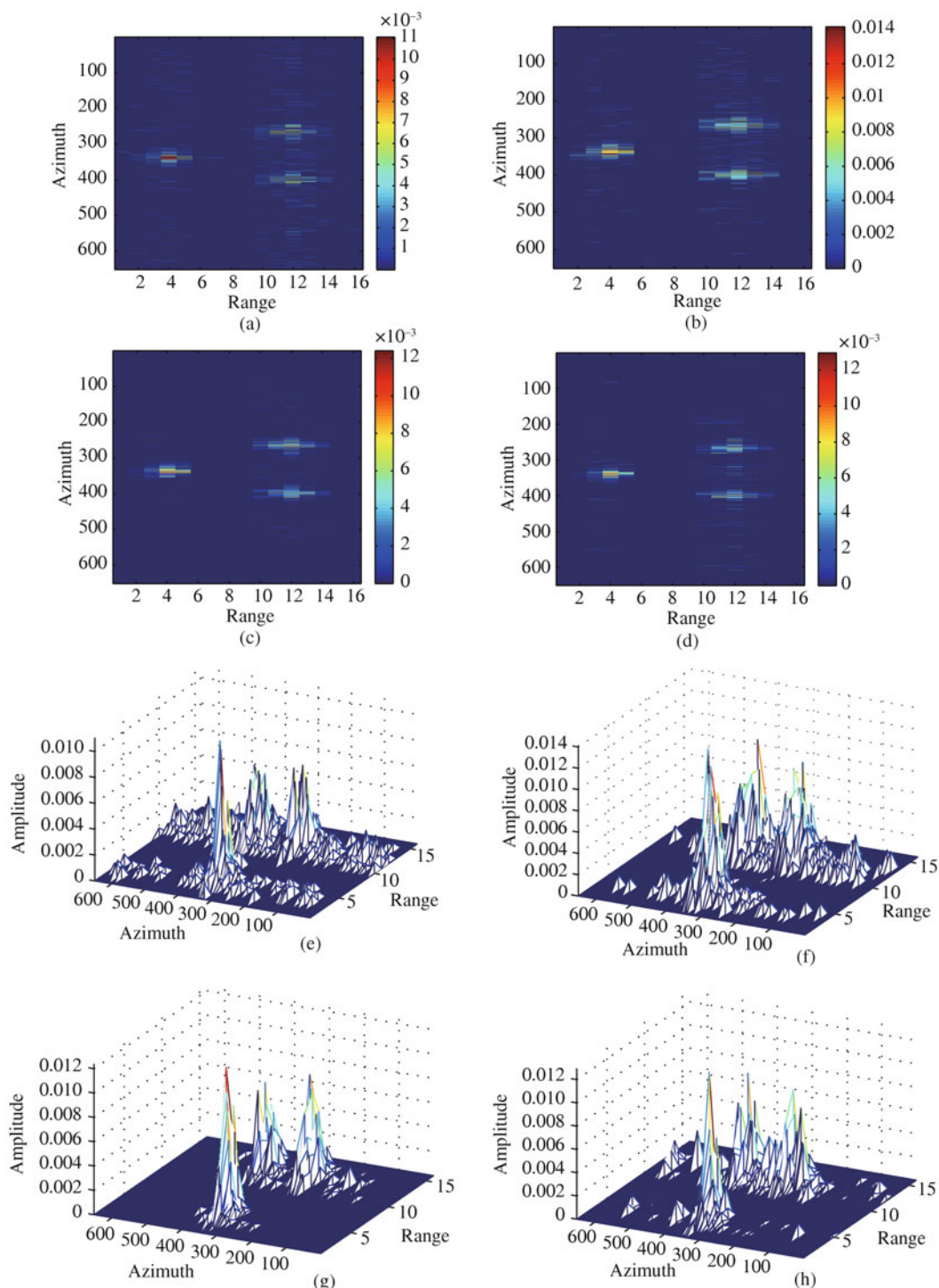
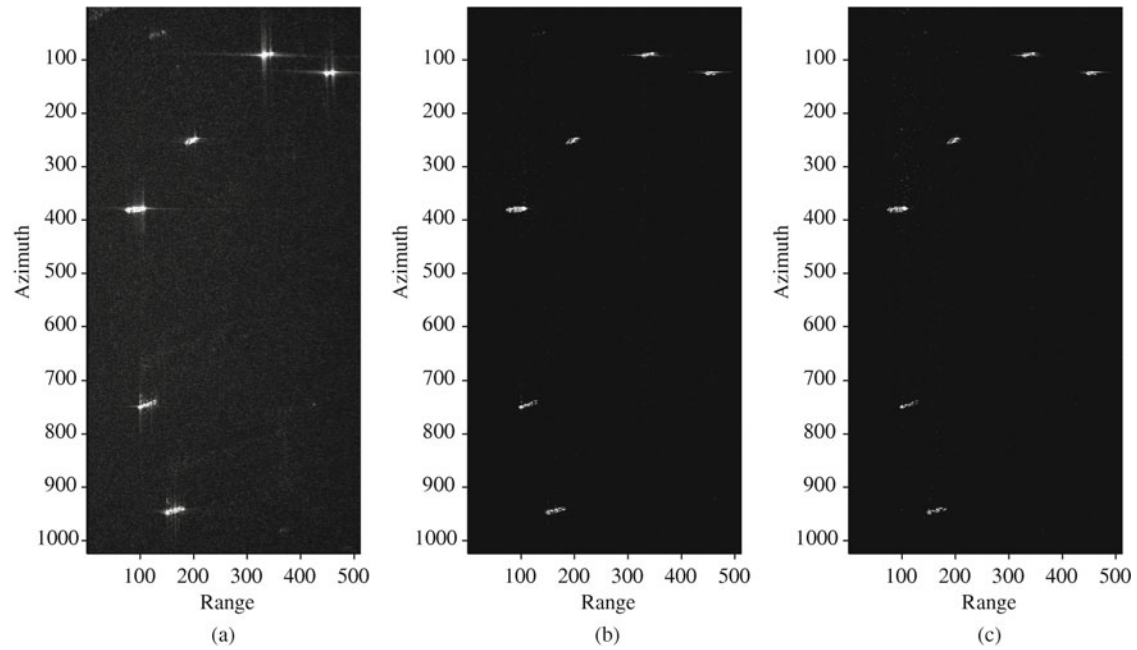


Figure 10 Reconstruction images of Ground-Based SAR data via OMP, L_1 regularization based and the new methods using different pulses. (a) OMP based SAR image using 130 pulses; (b) L_1 regularization based SAR image using 130 pulses; (c) $L_{1/2}$ -SAR image using 130 pulses; (d) $L_{1/2}$ -SAR image using 65 pulses; (e) mesh plot of the OMP based SAR image using 130 pulses; (f) mesh plot of the L_1 regularization based SAR image using 130 pulses; (g) mesh plot of the $L_{1/2}$ -SAR image using 130 pulses; (h) mesh plot of the $L_{1/2}$ -SAR image using 65 pulses.

As demonstrated by Figure 10, the new method outperforms the other sparse SAR imaging methods. On one hand, the new method produces the high-quality image with higher resolution, lower sidelobes and fewer artifacts, as shown in Figures 10 (c) and (g). On the other hand, the proposed method needs fewer measurements to implement SAR imaging effectively, as shown in Figures 10 (d) and (h).

Table 2 The running time of three sparse SAR imaging methods for GB-SAR data (unit: s)

Pulses	OMP	L_1 -SAR	$L_{1/2}$ -SAR
651	138.9500	79.22	79.25
130	21.0156	8.95	8.48
65	12.4700	5.45	5.70

**Figure 11** RADARSAT-1 data imaging results via RDA with full sampling and the proposed $L_{1/2}$ -SAR imaging method with undersampling. (a) The traditional radar image under the full sampling data; (b) $L_{1/2}$ -SAR image under the sampling rate 25%; (c) $L_{1/2}$ -SAR image under the sampling rate 12.5%.

4.2 RADARSAT-1 data reconstruction

We now show the application results for the data from RADARSAT-1 in the fine mode-2 about Vancouver region. In [32], the detailed target and data descriptions are provided. We are interested in the region of the English Bay, where there are six sitting vessels. The main radar parameters are set as follows: the signal bandwidth is 30.111 MHz, the pulse repetition frequency is 1256.98 Hz. The traditional SAR image via RDA under full sampling based on the Nyquist rate is shown in Figure 11(a), and the $L_{1/2}$ -SAR images reconstructed under 25% and 12.5% sampling rates are shown in Figures 11 (b) and (c), respectively. Furthermore, more detailed comparison between Figures 11 (a) and (b) is shown in Figure 12.

As compared with the traditional SAR reconstruction result, the proposed method reconstructs higher quality images with increased resolution and reduced sidelobes at much lower sampling rate than the Nyquist rate, as shown in Figure 11. More specifically, the proposed method implements SAR imaging effectively under 12.5% or even lower sampling rate, as demonstrated by Figure 11 (c) and Figures 13 (c), (f). These properties of the new method are further demonstrated by the comparison of the detailed information about the traditional SAR image and $L_{1/2}$ -SAR image at 25% sampling rate, as shown in Figure 12. There are higher sidelobes of the traditional SAR image as shown in the first row of Figure 12, while the sidelobes of the corresponding target regions are suppressed efficiently via $L_{1/2}$ -SAR imaging method, as demonstrated by the second row of Figure 12. Specially, there are significant improvements in the interested target regions 1, 2, 4 and 5, as shown in Figure 12. Moreover, the backgrounds of the target regions are much smoother with fewer artifacts.

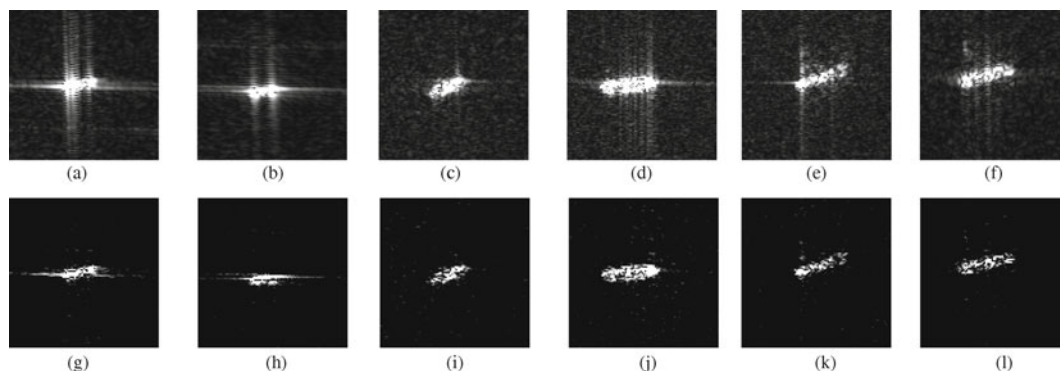


Figure 12 Detailed comparison between the traditional SAR image of RADARSAT-1 data (Figure 11 (a)) and $L_{1/2}$ -SAR image of RADARSAT-1 data under 25% sampling rate (Figure 11 (b)). Along the azimuth of the Figure 11 (a) (from top to bottom), the six interested targets are denoted by $T1$ to $T6$. All target regions with 101×101 pixels are enlarged to show the details explicitly. The first row of images represents the detailed targets information of the traditional image under the full sampling, and the second row of images represents the detailed targets information of $L_{1/2}$ -SAR image under 25% sampling rate. (a) $T1$ of the traditional SAR image; (b) $T2$ of the traditional SAR image; (c) $T3$ of the traditional SAR image; (d) $T4$ of the traditional SAR image; (e) $T5$ of the traditional SAR image; (f) $T6$ of the traditional SAR image. (g) $T1$ of $L_{1/2}$ -SAR image; (h) $T2$ of $L_{1/2}$ -SAR image. (i) $T3$ of $L_{1/2}$ -SAR image; (j) $T4$ of $L_{1/2}$ -SAR image; (k) $T5$ of $L_{1/2}$ -SAR image; (l) $T6$ of $L_{1/2}$ -SAR imaging.

Furthermore, we compared the new method with both OMP and L_1 regularization based methods. We applied these methods to the RADARSAT-1 data by the use of different sampling rates including 25%, 10%, 8%, and 5%. A part of the reconstruction results of these methods are shown in Figure 13. The corresponding running time of three sparse SAR imaging methods is shown in Table 3. As shown in Table 3, the new method is much faster than the OMP based method, and also faster than the L_1 regularization based SAR imaging method. More specifically, the running time of the new method is less than fifth of the OMP based method. In general, the running time of these sparse SAR imaging methods decreases as the sampling rate reduces.

As demonstrated by Figure 13, the outperformance of the new method is also supported as compared with the other sparse based SAR imaging methods. As shown in Figures 13 (a)–(c), when the sampling rate is 10%, the reconstruction of the new method is better than both OMP and L_1 regularization based methods. It is evident that there are many artifacts and sidelobes in the reconstructions of OMP and L_1 regularization based methods, as shown in Figures 13 (a) and (b). Moreover, when the sampling rate is further reduced to 5%, the reconstruction of the new method is still better than the other two methods in the sense of identification, and gives much clearer visual effect.

5 Conclusion

Through modeling SAR imaging problem into an $L_{1/2}$ regularization problem, which optimizes a quadratic error term of the SAR observation with the interested scene sparsity prior, we have suggested a new SAR imaging method based on the well-developed $L_{1/2}$ regularization theory. The suggested method implements SAR imaging in an iterative way, including a Landweber update step and a half thresholding operator step at each iteration. It can be explained as a finer update of the conventional matched filtering method, driven by the scene sparsity. Over the conventional SAR imaging techniques, the most remarkable advantage of the new method is the breakthrough of the limitation of the traditional Nyquist rate; that is, beyond Nyquist rate is sufficient for the new method to implement SAR imaging effectively. Specifically, the sampling rates sufficient to the new method are 30%, 20% and 10% for our conducted, GB-SAR and RADARSAT-1 data experiments, respectively. Another advantage of the new method is that it produces higher quality images with increased resolution and reduced sidelobes.

The advantages of the new method are also supported by comparison with the prevalent greedy pursuit and L_1 regularization based SAR imaging methods. The comparison shows that, on one hand, the new

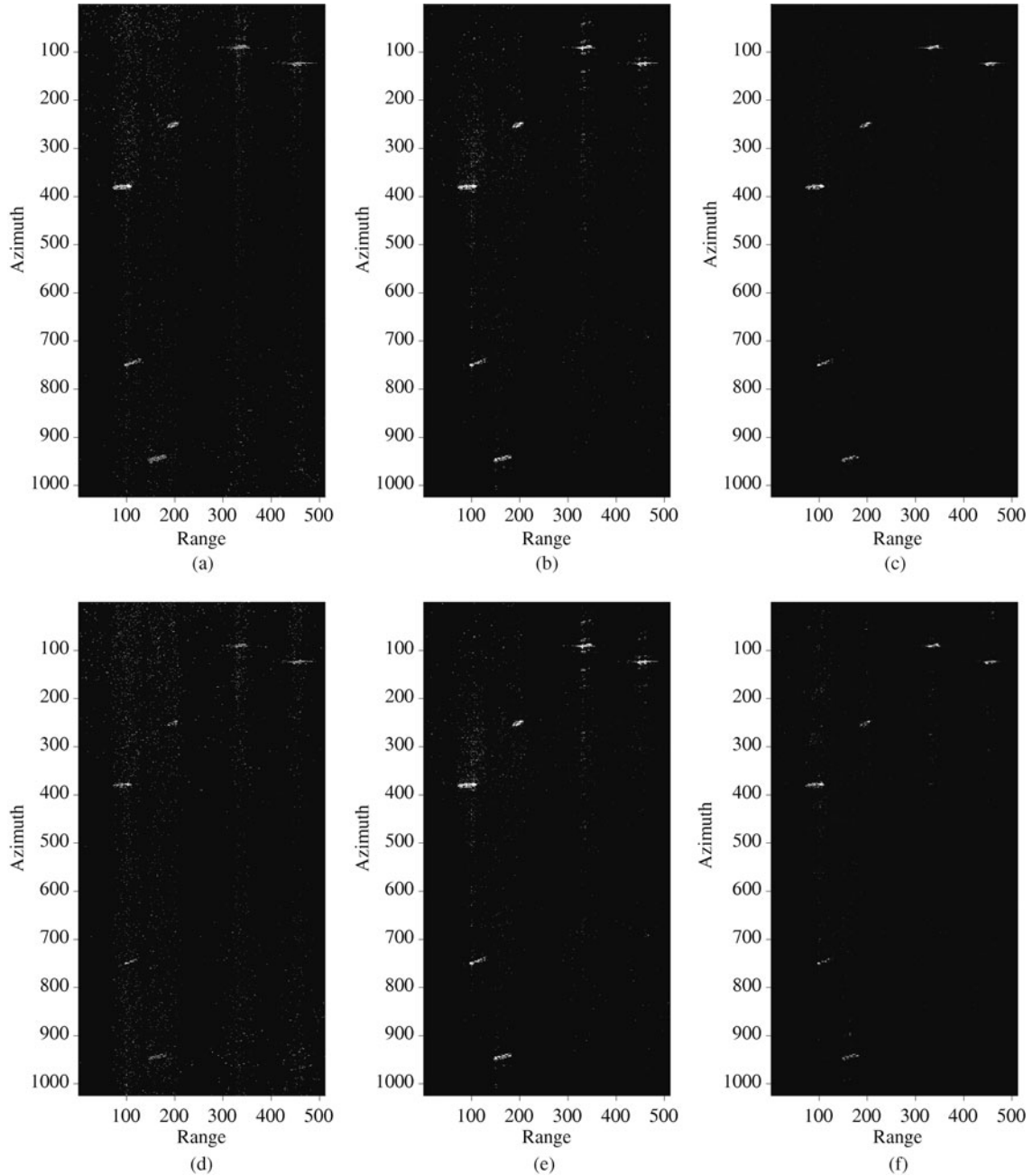


Figure 13 RADARSAT-1 data imaging results via OMP, L_1 regularization based and the new SAR imaging methods at different sampling rates; (a) the OMP base SAR image at sampling rate 10%; (b) L_1 -SAR image at sampling rate 10%; (c) $L_{1/2}$ -SAR image at sampling rate 10%; (d) the OMP base SAR image at sampling rate 5%; (e) L_1 -SAR image at sampling rate 5%; (f) $L_{1/2}$ -SAR image at sampling rate 5%.

Table 3 The running time of three sparse SAR imaging methods for RADARSAT-1 data (unit: s)

Sampling rate(%)	OMP	L_1 -SAR	$L_{1/2}$ -SAR
25	12403.20	1454.80	1240.22
10	5273.64	663.45	511.63
8	3578.59	534.58	454.98
5	1578.59	377.39	330.55

method has better sparse reconstruction ability than both greedy pursuit and L_1 regularization based methods, and there is a significant reduction of the sampling rate for SAR imaging, which is also demon-

strated by real SAR data experiments. There are more than 10% and 9% improvements of the new method compared to the OMP and L_1 regularization based methods, respectively, both in the noiseless and noise cases, in terms of the percentages of successful reconstruction regions. On the other hand, the new method is more robust to the data noise than both OMP and L_1 regularization based methods. More specifically, as demonstrated by Figure 7, the new method can reconstruct the original scene from noisy compressed measurements with lower SNR (about 5 dB reduction). Moreover, as demonstrated by the real SAR data experiments, the running time of the new method is much less than the OMP based method, and as fast as FISTA, which is a fast L_1 regularization algorithm.

The study in the present paper shows that the new method can be accepted as a new, efficient compressive sensing based SAR imaging way. We should notice, however, that the prerequisite of validity of the new method (actually, any compressive sensing based SAR imaging) is the sparsity existed in target scene. This is not always the case of course. A further study should go to looking for appropriate transformations such that under the transformations the target scene can have sparsity. Also, as demonstrated in the SAR observation process (1), (2), the observation matrix of SAR system, A , is directly dependent on the transmitted waveform (so is the reconstruction); therefore, the optimal transmitted waveform adapted to compressive sensing should be further designed.

Acknowledgements

This work was supported by Key Program of the National Natural Science Foundation of China (Grant No. 11131006), State Key Development Program for Basic Research of China (973 Program) (Grant No.2010CB-731905), and National Natural Science Foundations of China (Grant Nos. 61075054, 60975036, 11171272).

References

- 1 Curlander J C, McDonough R N. Synthetic Aperture Radar: Systems and Signal Processing. New York: Wiley, 1991
- 2 Rihaczek A W. Principles of High-Resolution Radar. New York: McGraw-Hill, 1968
- 3 Candes E, Romberg J, Tao T. Robust uncertainty principles: exact signal reconstruction from highly incomplete frequency information. *IEEE Trans Inf Theory*, 2006, 52: 489–509
- 4 Donoho D L. Compressed sensing. *IEEE Trans Inf Theory*, 2006, 52: 1289–1306
- 5 Alonso M T, Lopez-Dekker P, Mallorqui J J. A novel strategy for radar imaging based on compressive sensing. *IEEE Trans Geosci Remote Sens*, 2010, 48: 4285–4295
- 6 Baraniuk R, Steeghs P. Compressive radar imaging. In: *IEEE Radar Conference*, Waltham, 2007. 128–133
- 7 Potter L C, Ertin E, Parker J T, et al. Sparsity and compressed sensing in radar imaging. *Proc IEEE*, 2010, 98: 1006–1020
- 8 Tropp J A, Gilbert A. Signal recovery from random measurements via orthogonal matching pursuit. *IEEE Trans Inf Theory*, 2007, 53: 4655–4666
- 9 Needell D, Vershynin R. Signal recovery from incomplete and inaccurate measurements via regularized orthogonal matching pursuit. *IEEE J Sel Top Signal Process*, 2010, 4: 310–316
- 10 Tropp J A, Wright S. Computational methods for sparse solution of linear inverse problems. *Proc IEEE*, 2010, 98: 948–958
- 11 Cetin M, Karl W. Feature-enhanced synthetic aperture radar image formation based on nonquadratic regularization. *IEEE Trans Image Process*, 2001, 10: 623–631
- 12 Cetin M, Lanterman A. Region-enhanced passive radar imaging. *Proc Inst Elect Eng Radar Sonar Navig*, 2005, 152: 185–194
- 13 Lee J A C, Arikan O, Munson J D C. Formulation of a general imaging algorithm for high-resolution synthetic aperture radar. In: *IEEE International Conference On Acoustics, Speech and Signal Processing*, Atlanta, 1996. 2092–2095
- 14 Logan C L. An estimation-theoretic technique for motion-compensated synthetic-aperture array imaging. Ph.D. dissertation. Cambridge: Massachusetts Institute of Technology, 2000
- 15 Tikhonov A N. Solution of incorrectly formulated problems and the regularization method. *Soviet Math Dokl*, 1963, 4: 1035–1038
- 16 Tikhonov A N, Arsenin V Y. *Solutions of Ill-Posed Problems*. Washington: Winston, 1977
- 17 Beck A, Teboulle M. A fast iterative shrinkage-thresholding algorithm for linear inverse problems. *SIAM J Imag Sci*, 2009, 2: 183–202
- 18 Candes E, Romberg J, Tao T. Stable signal recovery from incomplete and inaccurate measurements. *Commun Pure*

- Appl Math, 2006, 59: 1207–1223
- 19 Donoho D L, Elad M, Temlyakov V N. Stable recovery of sparse overcomplete representations in the presence of noise. *IEEE Trans Inf Theory*, 2006, 52: 6–18
 - 20 Duabecheies I, Defrise M, Mol C. An iterative thresholding algorithm for linear inverse problems with a sparse constraint. *Commun Pure Appl Math*, 2004, 57: 1413–1457
 - 21 Donoho D L. High-dimensional centrally symmetric polytopes with neighborliness proportional to dimension. *Discret Comput Geom*, 2006, 35: 617–652
 - 22 Donoho D L, Tanner J. Observed universality of phase transitions in high-dimensional geometry, with applications in modern signal processing and data analysis. *Philos Trans Royal Soc A*, 2009, 367: 4273–4293
 - 23 Chartrand R, Staneva V. Restricted isometry properties and nonconvex compressiv sensing. *Inverse Probl*, 2008, 24: 1–14
 - 24 Xu Z B, Zhang H, Wang Y, et al. $L_{\frac{1}{2}}$ regularizer. *Sci China Inf Sci*, 2010, 53: 1159–1169
 - 25 Xu Z B, Chang X Y, Xu F M, et al. $L_{1/2}$ Reguralization: a thresholding representation theory and a fast solver. *IEEE Trans Neural Netw Learn Syst*, 2011 (in press)
 - 26 Xu Z B, Guo H L, Wang Y, et al. The representation of $L_{1/2}$ regularizer among $L_q(0 < q < 1)$ regularizer: an experimental study based on phase diagram. *Acta Autom Sin*, 2011 (in press)
 - 27 Xu Z B. Data modeling: Visual psychology approach and $L_{1/2}$ regularization theory. In: *Proceedings of International Congress of Mathematicians, Hyderabad, 2010*. 3153–3184
 - 28 Zweig G. Super-resolution Fourier transforms by optimisation, and ISAR imaging. *IEE Proc Radar Sonar Navig*, 2003, 150: 247–252
 - 29 Zhang H, Guo H L, Liang Y, et al. The essential ability of sparse reconstruction of different compressive sensing strategies. *Sci China Inf Sci*, 2011, doi:10.1007/s11432-011-4502-6
 - 30 Wu C. A digital system to produce imagery from SAR data. In: *AIAA Conference: System Disign Driven by Sensors*, Pasadena, 1976
 - 31 Wu C. Procesing of SEASAT Data. In: *SAR Technology Symp*, Las Cruces, 1977
 - 32 Cumming I G, Wong F H. Digital processing of synthetic aperture radar data: algorithms and implementation. MA: Artech House, 2004